Published in final edited form as:
Invest Ophthalmol Vis Sci. 2008 April ; 49(4): 1571–1579. doi:10.1167/iovs.07-0838.

Characterization of Outer Retinal Morphology with High-Speed, Ultrahigh-Resolution Optical Coherence Tomography

Vivek J. Srinivasan[1], **Bryan K. Monson**[2], **Maciej Wojtkowski**[1,2,3], **Richard A. Bilonick**[4], **Iwona Gorczynska**[1,2], **Royce Chen**[2], **Jay S. Duker**[2], **Joel S. Schuman**[4], and **James G. Fujimoto**[1]

[1]Department of Electrical Engineering and Computer Science and Research Laboratory of Electronics, Massachusetts Institute of Technology, Cambridge, Massachusetts

[2]New England Eye Center, Tufts-New England Medical Center, Tufts University, Boston, Massachusetts

[4]UPMC Eye Center, Department of Ophthalmology, University of Pittsburgh School of Medicine, Pittsburgh, Pennsylvania.

Abstract

Purpose—To visualize, quantitatively assess, and interpret outer retinal morphology by using high-speed, ultrahigh-resolution (UHR) OCT.

Methods—Retinal imaging was performed in the ophthalmic clinic in a cross-section of 43 normal subjects with a 3.5-μm, axial-resolution, high-speed, UHR OCT prototype instrument, using a radial scan pattern (24 images, 1500 axial scans). Outer retinal layers were automatically segmented and measured. High-definition imaging was performed with a 2.8-μm axial-resolution, high-speed, UHR OCT research prototype instrument, to visualize the finer features in the outer retina.

Results—Quantitative maps of outer retinal layers showed clear differences between the cone-dominated fovea and the rod-dominated parafovea and perifovea, indicating that photoreceptor morphology can explain the appearance of the outer retina in high-speed, UHR OCT images. Finer, scattering bands were visualized in the outer retina using high-definition imaging and were interpreted by comparison to known anatomy.

Conclusions—High-speed UHR OCT enables quantification of scattering layers in the outer retina. An interpretation of these features is presented and supported by quantitative measurements in normal subjects and comparison with known anatomy. The thick scattering region of the outer retina previously attributed to the retinal pigment epithelium (RPE) is shown to consist of distinct scattering bands corresponding to the photoreceptor outer segment tips, RPE, and Bruch's membrane. These results may advance understanding of the outer retinal appearance in OCT images. The normative measurements may also aid in future investigations of outer retinal changes in age-related macular degeneration and other diseases.

Optical coherence tomography (OCT) is a medical imaging technology that can perform high resolution, cross-sectional imaging of tissue morphology in situ and in real time.1 It can provide

Corresponding author: James G. Fujimoto, Department of Electrical Engineering and Computer Science and, Research Laboratory of Electronics, Massachusetts Institute of Technology, 77 Massachusetts Avenue, Cambridge, MA 02139; jgfuji@mit.edu. .
[3]Present affiliation: Institute of Physics, Nicolaus Copernicus University, Toruń, Poland.

Presented at the annual meeting of the Association for Research in Vision and Ophthalmology, Fort Lauderdale, Florida, May, 2006.

Disclosure: **V.J. Srinivasan**, None; **B.K. Monson**, None; **M. Wojtkowski**, None; **R.A. Bilonick**, None; **I. Gorczynska**, None; **R. Chen**, None; **J.S. Duker**, None; **J.S. Schuman**, P; **J.G. Fujimoto**, P

detailed images and quantitative information about retinal structure and has therefore become a standard diagnostic technique in ophthalmology.2,3 The StratusOCT system (Carl Zeiss Meditec, Inc., Dublin, CA), with an 8- to 10-μm axial image resolution, can provide detailed cross-sectional images of retinal disease and quantitative measurements, including macular thickness, nerve fiber layer thickness, and optic nerve head topography. Normative databases for macular thickness and nerve fiber layer thickness are available to aid in the interpretation of quantitative measurements. Analysis of finer intraretinal structures has been difficult because of speed and resolution limitations. However, segmentation of the inner retinal complex, outer plexiform layer, and outer retinal complex in StratusOCT images has recently been demonstrated.[4] Another study demonstrated foveal photoreceptor layer changes in central serous chorioretinopathy that correlate with visual acuity loss.[5] Recently, a correlation between macular hole postoperative visual acuity and photoreceptor thickness measured manually from StratusOCT images has been shown.[6]

Ultrahigh-resolution (UHR) OCT imaging with axial resolutions of 2 to 3 μm was demonstrated to improve significantly the visualization of normal retinal morphology[7,8] and retinal disease[9–14] Although conventional UHR OCT systems that use time domain detection enable visualization of structural detail in the outer retina, quantitative mapping with conventional UHR OCT technology has been difficult, because of imaging speed limitations and consequent motion artifacts. Nevertheless, several studies have been performed in which photoreceptor thickness was measured manually on a small number of images. One study correlated photoreceptor loss and foveal thickness with visual acuity in Stargardt disease-fundus flavimaculatus.[12] In another study, central foveal photoreceptor thickness measured by UHR OCT was correlated with visual acuity in retinitis pigmentosa and degenerative diseases.[14] To date, comprehensive quantitative mapping of the photoreceptors and RPE has not been possible with conventional UHR OCT, due to motion artifacts and limited retinal coverage.

Recently, advances in OCT technology have enabled UHR OCT imaging with a ~50× increase in imaging speed over standard resolution OCT systems and a ~100× increase in imaging speed over previous UHR OCT systems.[15–17] These techniques are based on “spectral” or “Fourier domain” detection, where echo time delays of light are measured by acquiring the interference spectrum of the light signal and taking its Fourier transform.[18,19] Since all the light echoes from different axial depths are measured simultaneously, sensitivity and imaging speed are dramatically increased.[20–22] With increased imaging speed, individual images are acquired within a fraction of a second and depict the true retinal topography. Multiple images may be rapidly acquired at different locations or orientations, enabling three-dimensional imaging.[23,24] The number of axial scans per image may be increased significantly, to obtain high-definition images.[25] Adaptive optics has also been combined with high-speed OCT, to visualize the cone photoreceptors in three dimensions.[26]

In this study, high-speed UHR OCT was used for the visualization, measurement and mapping of outer retinal morphology in normal subjects. OCT imaging was performed with a 3.5-μm axial-resolution prototype instrument using a radial scan pattern, and scattering bands in the outer retina were measured and mapped in 43 normal subjects of various ages. Quantitative maps were used to assign these bands to specific outer retinal layers or features based on comparison with the known topographic distribution of cones and rods in the macula. The cross-sectional relationships between layer measurements and age were also investigated. In addition, high-definition imaging was performed with a 2.8-μm axial-resolution prototype instrument to visualize finer bands in the outer retina. Anatomic correlates for these more subtle outer retinal features were determined.

Methods

Two research prototype UHR OCT systems with axial image resolutions of 3.5 and 2.8 μm, respectively, were developed and used in the study. Both systems had transverse resolutions of 20 to 25 μm. The axial resolution in OCT is determined by the coherence length of the light source, which is inversely proportional to the bandwidth ($\Delta\lambda$). For quantitative mapping, imaging was performed at the New England Eye Center (Boston, MA) with a high-speed, UHR research prototype system using a multiplexed superluminescent diode (SLD) light source (λ = 840 nm, $\Delta\lambda$ = 95 nm; Broadlighter T40-HP2; Superlum Ltd., Carrigtwohill, Ireland). Because of the modulations in the SLD spectrum, digital spectral shaping was necessary to reduce sidelobes in the point-spread function.[27] Digital spectral shaping multiplies the detected spectrum by a correction function, to obtain an approximately Gaussian shape. The axial image resolution was 3.5 μm in tissue, after digital spectral shaping, assuming an index of refraction of 1.4. This system used a spectrometer with a 2048-pixel CCD camera and operated at 24,000 axial scans per second.[17]

Seventy-four eyes of 45 subjects were imaged with high-speed UHR OCT. In 29 subjects both eyes were imaged, whereas in the remaining 16, a randomly chosen eye was imaged. Four eyes of three subjects were excluded because of low signal and poor image quality. The criterion for exclusion was that the vitreoretinal interface was not visible across all images. Seventy eyes of 43 normal subjects were included for quantitative analysis (mean age, 42.7 ± 17.4 years; range, 19 – 81). Of the 70 eyes, 36 were right and 34 were left. Of the 43 subjects, there were 28 females; 8 were non-Caucasian. Normal eyes were determined on the basis of standard ophthalmic examination and history. The study was approved by the institutional review board committees of both the Massachusetts Institute of Technology and Tufts-New England Medical Center. Written informed consent was obtained from all subjects before OCT imaging was performed. The research adhered to the tenets of the Declaration of Helsinki.

A radial scanning pattern with 24 images (6 mm, 1500 axial scans per image, with a 1.5-second acquisition time) centered on the fovea was developed to map outer retinal morphology (Fig. 1A). Care was taken to ensure that the radial scanning pattern was centered on the fixation target. Compared with a raster scanning pattern which typically has ~500 axial scans per image, this radial scanning pattern has more axial scans per image, which yields improved image quality. Mapping is also possible by processing a relatively small set of images. Given the expected circular symmetry of the outer retinal morphology at low eccentricities,[28] the radial scanning protocol was expected to be a more efficient approach for the study, which maps the macula.

Eye motion and centration errors are important factors that may invalidate clinical data. A radial scanning protocol reduces eye motion artifacts compared with a raster scan. A raster of 180 images with 500 axial scans per image requires an acquisition time of ~4 seconds. Although OCT imaging is performed at 840 nm, the OCT beam is visible to the subject. During a raster scan, the subject's gaze may track the scanning pattern along the slow axis of the raster scan. The radial pattern is less distracting to the subjects because, in addition to being faster, all scans intercept the center of fixation. However, the radial scanning pattern has the disadvantage that it is not possible to generate a high-quality OCT fundus image[29–31] to assess motion. Eye motion during the acquisition of a single image is possible but unlikely, because of the high scanning speed (63 ms for one image). Eye motion during the entire scan protocol is much more likely and cannot currently be corrected with this prototype. It was the responsibility of the instrument operator to ensure stable fixation by the subject and to ensure data integrity. To confirm that excessive eye motion did not occur and to compensate for fixation errors, the position of minimum retinal thickness in each of the 24 radial images was measured and used

to register the images. This approach has the limitation that it works only in eyes with a normal foveal contour.

Segmentation software detected the external limiting membrane (ELM), the photoreceptor inner segment/outer segment junction (IS/OS) inner and outer boundaries, the inner boundary of the cone outer segment (COS) tips, the outer boundary of Bruch's membrane (BM), and the vitreoretinal interface (VRI), as shown in Figure 1C. Four morphologic features were quantified by measuring the distance between different boundaries (Fig. 1D). The features quantified were IS length, COS length; combined rod outer segment tips (ROSTs), cone outer segment tips (COSTs), and retinal pigment epithelium/BM (OS tips and RPE/BM); and combined total outer segment and RPE/BM (total OS and RPE/BM). A refractive index of 1.4 was assumed in thickness calculations. Thicknesses were averaged over annular regions, with increments of 0.75-mm diameter centered on the foveola. The interpretation of the outer retinal bands is discussed in detail in the Discussion section.

The segmentation algorithm used was a modification of that described by Koozekanani et al.[32] The VRI, IS/OS junction inner boundary and BM outer boundary were determined first. The locations of these high-contrast boundaries were used to place constraints on the locations of other boundaries of interest. The ELM was constrained to between 10 and 35 μm proximal to the IS/OS junction. The IS/OS junction outer boundary and COSTs inner boundary were constrained to between the IS/OS junction inner boundary and BM outer boundary.

Before segmentation, images were median filtered by 3 pixels in the transverse direction and down sampled to consist of 500 transverse pixels. Because of the high axial scan density, this step did not result in a loss of transverse resolution. All boundaries except the ELM had to occur at 0 crossings of the second derivative of the linear image. Therefore, the following criterion was used:

$$s_{zc}=\text{zero crossings}\left(g''*A\right),$$

where g is a Gaussian kernel, where the optimal width of the kernel was determined empirically for each boundary and was the same for all measured eyes. A is the median filtered axial scan. The overall edge strength criterion for each boundary except the ELM could be expressed as

$$\begin{aligned} s_{zc}=\text{zero crossings}\left(g''*A\right)\, s=s_{zc}\times(\pm g'*A) \\ \times(h_1*A)^{n_1} \\ \times(h_2*A)^{n_2}. \end{aligned}$$

For each axial scan, the maximum value of s determined the initial estimate for the boundary. In the expression, * denotes convolution along the axial direction, × denotes multiplication, and s is the product of four terms, which represent the four criteria that must be satisfied for the boundary of interest. The first-term s_{zc} selects 0 crossings of g" * A. The second term ±g' * A weights regions where the derivative along the axial direction is large in magnitude and has the desired sign. The positive sign is chosen for positive-going boundaries (VRI, IS/OS inner boundary, and COSTs boundary), and the negative sign is chosen for negative-going boundaries (IS/OS outer boundary and BM outer boundary). The kernels h_1 and h_2 are causal and anticausal functions used to select regions proximal and distal the boundary, respectively. Depending on the signs of n_1 and n_2, the last two terms weight boundaries near regions of either high (positive sign) or low reflectivity (negative sign). The magnitudes of n_1 and n_2 determine the relative weighting of the different terms. For instance, the VRI boundary must be distal to

a region of low reflectivity corresponding to the vitreous; therefore, for this case $n_1 = -4$ and h_1 was a causal rectangular kernel. The VRI boundary must be proximal to a region of high reflectivity corresponding mostly to the nerve fiber layer (NFL), therefore for this case $n_2 = 1$ and h_2 was an anticausal rectangular kernel. The shapes of the kernels h_1 and h_2 and the values of n_1 and n_2 were determined empirically for each boundary and were the same for all measured eyes. In order to detect the ELM, the median-filtered image was used directly to search for a thin reflective line between 10 and 35 μm proximal to the IS/OS junction.

The edge strength criteria described typically resulted in relatively good initial estimates of the boundaries. However, refining of boundary estimates was necessary for accurate segmentation. A jump of greater than 28 μm for the VRI (14 μm for all other boundaries) was defined as a segmentation error. Starting from the largest continuous segment with no errors, linear interpolation was used to correct segmentation errors in boundaries, similar to the procedure described previously.[32] All segmentation was fully automated and did not require operator assistance. In many subjects, vignetting and the directionality of photoreceptor backreflection caused increased segmentation error at eccentricities of $r > 1.25$ mm, particularly in detection of the COSTs inner boundary. In these subjects, the COST band appeared more diffuse and poorly defined at larger eccentricities, which caused detection of the inner boundary distal to its actual location. Therefore, quantitative analysis was limited to eccentricities of $r < 1.5$ mm. However, accurate segmentation was possible over the entire 6-mm diameter region in ~40% of the subjects. Segmentation results from all 70 eyes over the 3-mm diameter region ($r < 1.5$ mm) were included in the analysis. Accuracy of segmentation was assessed by comparing fully automated measurements to manually assisted measurements performed on a subset of the data. In addition, all 1680 segmented images were checked by an expert observer, and segmentation results were determined to be accurate over this region, with minor segmentation errors.

A linear mixed-effects model was used to determine how measurements of outer retinal features varied with eccentricity, while accounting for fixed effects due to differences in subjects' ages, random differences among subjects, and the correlation of eyes within subjects. Variance components included a random intercept for subjects and a random interaction between subjects and features which were assumed to be uncorrelated. To account for the correlation among residuals (error estimates) for various distances, we used an autoregressive moving average correlation structure of order $P = 1$ and $q = 1$. The residual error variance was allowed to vary with the feature and may help account for the differences in segmentation accuracy of different boundaries, which results in residual error variances that are different for different features (heteroskedasticity).

A large number of potential models were investigated, including those with random distance slopes for subjects and for the interaction between subjects and features. These variance components were negligible and eliminated. A variance component for eyes within subjects was also investigated but was found to be negligible. The Akaike information criterion (AIC) was used to select the optimal model, which included linear and quadratic terms for eccentricity and age.

An additional UHR OCT prototype instrument was developed at MIT for high-definition retinal imaging and was used to aid in the interpretation of outer retinal layers. A spectrometer with a telecentric lens and 4,096 pixel line scan CCD camera operating at 12,000 axial scans per second was used. A broader bandwidth multiplexed SLD source ($\lambda = 890$ nm, $\Delta\lambda = 150$ nm; Broadlighter D890; Superlum Ltd.) enabled an axial image resolution of 2.8 μm in tissue after digital spectral shaping, which compensated for water absorption in the vitreous. Compared with the prototype system at the New England Eye Center, which has a 3.5-μm axial image resolution, this instrument had higher resolution at the expense of a 2× reduction in imaging

speed. This system was used only for acquisition of the high-definition retinal images shown in Figures 4 and 5.

Results

Figure 2 shows the average dimensions of the retina, obtained by averaging measurements over all subjects. Figure 2A shows a radial plot of average dimensions of the outer retina. The horizontal axis represents distance from the foveal center, and the vertical axis represents the average thickness at a given distance from the foveal center. Even though the VRI is not perfectly circularly symmetric about the foveal center, it is shown on the radial plot to visualize the approximate foveal contour. Figure 2B shows the average outer retinal thickness maps, averaged over all subjects. These maps appear symmetric, justifying the radial plot in Figure 2A. Figure 3 shows the thickness measurements, grouped according to annular region (columns) and measured feature (rows). The fit obtained from the linear mixed-effects model is shown. Table 1 shows the parameter estimates from the linear mixed-effects model. All measurements have negative linear distance slopes ($\beta_{1,dist} < 0$) and positive quadratic distance slopes ($\beta_{2,dist} > 0$), with the exception of the OS tips and RPE/BM measurement, which has a positive linear distance slope ($\beta_{1,dist} > 0$) and a negative quadratic distance slope ($\beta_{2,dist} < 0$). The IS length measurement and the total OS and RPE/BM measurement have a relatively weak distance curvature, whereas the distance curvatures for the COS length measurement and the OS tips and RPE/BM measurement are strong. Finally, the IS length measurement shows an approximately linear decrease with age. The COS length measurement and the OS tips and RPE/BM measurement increase and decrease with age, respectively, with the overall pattern showing curvature. The total OS and RPE/BM measurement exhibit a strong curvature with age. The residual model errors (standard deviations) are COS length, 2.19 μm; IS length, 0.84 μm; OS tips and RPE/BM measurement, 2.22 μm; and total OS and RPE/BM measurement, 1.77 μm.

Possible eye-motion artifacts and centration errors were evaluated by analyzing measurements from all subjects. The radial scanning pattern consisted of 24 scans in a spoke pattern, which generated 24 cross-sectional OCT images. Transverse displacements parallel to the scan and perpendicular to the scan were assessed. The location of the minimum retinal thickness in each image was used to determine displacement error of the scan center relative to the foveal center along the scan direction. The SD of the transverse displacement along the scan direction was 65 μm. The variation in the minimum retinal thickness among images from a given eye was used to estimate transverse displacement perpendicular to the scan direction. The minimum retinal thickness had an SD of 5.3 μm. Referring to Figure 2A, this corresponds to a transverse displacement of ~68 μm SD in the direction perpendicular to the scan, indicating that eye motion during the acquisition was small.

Segmentation accuracy was assessed quantitatively by comparing automated measurements to measurements obtained with an earlier software version that was manually assisted. The earlier software version did not measure IS length, and eccentricities were limited to $r < 1.13$ mm. Therefore, only three measurements (COS length, OS tips and RPE/BM, and total OS and RPE/BM) and three annular regions were analyzed quantitatively for accuracy. The differences (±SD) between the manual and automated measurements, in order of increasing eccentricity, were −4.2 ± 0.9, −4.6 ± 0.5, and −4.0 ± 0.8 μm for COS length; 1.1 ±1.2, 1.2 ± 0.9, and 0.5 ± 1.0 μm for the OS tips and RPE/BM measurement; and −3.1 ±1.0, −3.4 ± 0.9, and −3.5 ± 0.9 μm for the total OS and RPE/BM measurement. All segmented images were checked qualitatively by an expert observer, to further ensure that segmentation was accurate.

High-definition, UHR OCT imaging of normal retinas with 2.8-μm resolution was performed to aid in the interpretation of the outer retinal layers. Figure 4 shows a fundus photograph (Fig.

4A) and OCT image (Fig. 4B) of the papillomacular axis of the retina of a normal 28-year-old man, showing the transition from the fovea to the periphery. The IS, COS, ROS, and RPE—BM complex are labeled (Fig. 4C). Representative histologic sections from the human foveola (Fig. 4D) and near periphery (Fig. 4E) are compared with the corresponding regions shown on the papillomacular image. Histologic images are reproduced with permission.[28] To compare the parafovea and periphery, Figures 5A and 5B show, in a normal 24-year-old man, cross-sectional images of the retina located 1.5 and 5.2 mm from the foveal center, respectively.

Discussion

High-speed UHR OCT has enabled visualization of the outer retina with unprecedented detail. The outer retinal morphology visualized on conventional UHR OCT retinal images has been interpreted according to known histologic features.[33,34] Several clinical UHR OCT studies have described outer retinal changes in retinal diseases, which also suggest interpretations for the outer retinal layers based on known pathogenesis.[9,10,13] In the present study, quantitative measurements of outer retinal morphology are performed in vivo in normal human subjects and compared to known photoreceptor morphology in the macula.

Quantitative histologic comparisons are difficult because of processing artifacts, which are most severe in the OS when formalin or paraformaldehyde fixation and paraffin embedding are used.[35] In addition, contrast in OCT is produced by differences in refractive index and scattering properties of different tissues, as opposed to staining used in histology and light microscopy. Despite these limitations, UHR OCT measurements of outer retinal morphology agree reasonably well with those obtained from histology. Previous histologic studies measured outer retinal dimensions in a 37-year-old and a 72-year-old retina.[28,36] In the 37-year-old retina the IS were 30 to 35 μm in the foveola and 23 to 25 μm on the foveal slope outside the rod-free zone. Outer segments were 41 to 50 μm in the foveola and 25 to 31 μm along the foveal slope outside the rod-free zone. In the 72-year-old retina, the IS were 23 to 27 μm in the foveola and 27 to 33 μm along the foveal slope outside the rod-free zone. Outer segments were 57 to 63 μm in the foveola and 33 to 45 μm along the foveal slope outside the rod-free zone. In the parafovea at 1 mm eccentricity, COS lengths of 28 μm were measured in a 37-year-old retina. The authors noted that the photoreceptors in the 72-year-old retina at this eccentricity are similar to younger adults; however, the OS may be slightly longer.[28] Finally, at 4 mm eccentricity, ROS length was reported as 40 to 45 μm, whereas COS were approximately half this length. The authors reported that the OS of the 72-year-old retina were slightly shorter than those of the 37-year-old retina at this eccentricity.

The quantitative results presented in Figures 2 and 3 are in agreement with these histologic studies, accounting for the IS/OS junction thickness of ~12 μm (Fig. 2). This supports our interpretation of the more prominent outer retinal features and motivates further inspection of the more subtle bands within the region labeled OS tips and RPE/BM. We propose that the finer bands correspond to the COSTs, ROSTs, RPE, and BM.

Figure 4B shows a high-speed UHR OCT papillomacular image, with the outer retinal layers labeled in Figure 4C. A comparison of this image with known photoreceptor morphology supports our interpretation of the scattering bands in the outer retina. As expected, rods are absent in the foveola, where the cones extend to the RPE apical surface (Fig. 4D).[28] COS length is greatest in the foveola and decreases with increasing eccentricity (Fig. 4C), where the COSTs are displaced proximally from the RPE (Fig. 4E).[37] In Figure 4E, peripheral ROS interdigitate with the RPE and are visibly longer than peripheral cones.[37] Figure 5 further confirms the shortening of the cones in the periphery compared with the parafovea. In the peripheral image (Fig. 5B), the COSTs are clearly separate from the ROSTs and the RPE. The shortening of COS and the thickening of the OS tips and RPE/BM band with increasing distance from the

foveal center are confirmed by the model parameter estimates (Table 1) and are shown visually in Figure 2. A reduction in IS length with increasing distance from the foveal center is visualized in Figure 4 and confirmed by the model parameter estimates in Table 1. Studies of the macaque retina have shown that IS length decreases from the fovea to the parafovea and further decreases toward the periphery,[38] although histology of adult human retinas has shown conflicting results.[36]

The interpretation of the outer retina presented herein is consistent with known optical properties of the photoreceptors and previous work correlating histology and UHR OCT. In Figure 5, retinal layers are compared in the parafovea and periphery. In the inner retina, the NFL, ganglion cell layer (GCL), inner plexiform layer (IPL), inner nuclear layer (INL), outer plexiform layer (OPL), and outer nuclear layer (ONL) are visualized. At the posterior boundary of the ONL is the ELM. This thin reflective line may be due to microvillus Müller cell processes.[33] Posterior to the ELM, a reflective band represents the IS/OS junction of the photoreceptors, attributed to the IS ellipsoid which contains mitochondria.33 Posterior to the IS/OS junction band are the COSTs. This finding has recently been suggested in an elegant adaptive optics, high-speed OCT study, which showed a correlation between the COSTs layer and the IS/OS junction layer.26 According to this interpretation, the distance between IS/OS and COSTs bands should provide a good approximation for the COS length. Posterior to the COSTs is an additional band of high reflectance that corresponds to the ROSTs and possibly the apical RPE processes, which interdigitate with the ROS. This band appears to be absent in the fovea (Fig. 4D). At the distal end of the retina are the RPE and BM. The thickness of BM was measured in Figure 5A as 5.4 μm (full width at half maximum). Assuming a 2.8 μm axial image resolution, deconvolution of the image with the axial point spread function yields an estimated thickness of ~4.6 μm for BM. Posterior to BM are the choriocapillaris (CC) and choroid.

To provide further support for our interpretation of the retinal layers, a case of acute central serous chorioretinopathy (Figs. 6A, 6B) is shown, in which the OS were lifted from the RPE surface by subretinal serous fluid (Fig. 6C). In the parafovea, all bands were visible in the outer retina. At ~1.5 mm distance from the foveal center, the retina was separated from the RPE by the serous fluid. As expected, all bands assigned to the retina were elevated in the OCT image. Both the IS/OS and COSTs exhibited highly directional reflectance (Fig. 6D) and appeared diffuse in the region where the retina was elevated, which is expected based on the Stiles-Crawford effect. The two outermost bands, assigned to the RPE and BM, were not elevated by the serous fluid.

Our results show a cross-sectional relationship between outer retinal morphology and age (Table 1, Fig. 3). The data in Figure 3 show that the COS length was increased, while the IS length and the OS tips and RPE/BM measurement was decreased in older retinas. Previous research found longer COS in a 73-year-old than in a 37-year-old, which is consistent with our measurements.[36] Age-related changes in spatial density, phagocytic rate, directionality, optical properties, or positioning of the OS relative to the RPE, may also account for the observed cross-sectional relationships. Changes in rod density with age in the central retina have been reported, although cone density was stable.[39] A relationship between IS length and age has not been reported to our knowledge, although investigators in one study found age-related changes in IS diameter and coverage.[39]

In interpreting the results, it is important to recognize that age was measured cross-sectionally and not longitudinally. Therefore, changes attributed to age may be due to other factors that varied between subjects but were not controlled for. Sex and race were investigated as possible covariates, but were not statistically significant. More comprehensive studies including

investigations on larger subject populations and longitudinal studies are needed to confirm the presence of age-related changes in photoreceptor morphology.

Quantification of outer retinal morphology may become important in the diagnosis and management of diseases affecting the photoreceptors and the RPE. UHR OCT has the potential to reveal features of dry age-related macular degeneration (AMD) that provide information about the pathogenesis of this disease beyond the scope of standard clinical examination. In the future, it may be possible to identify and quantify high-risk markers for progression of AMD, such as BM thickening and photoreceptor changes.[40,41] Our results suggest that because of the close relationship between the photoreceptor OS tips, RPE, and BM, direct measurement of the RPE and BM may be difficult. In standard-resolution OCT images, the OS tips and RPE—BM band typically appear as a single scattering region and are often labeled RPE. The large measured thickness (~30–40 μm) of this band (Figs. 2, 3) can be attributed to the fact that it includes reflectance components from the photoreceptor OS tips in addition to scattering from the RPE and BM. Further improvements in software and axial resolution are necessary before BM and the RPE can be quantified directly in a clinical setting.

In conclusion, mapping of outer retinal morphology was demonstrated in normal subjects using high-speed, UHR OCT. Quantitative measurements were used to aid interpretation of the scattering bands visualized on UHR OCT images. Using high-definition imaging, the thick scattering region posterior to the IS/OS junction, previously attributed to the RPE, was shown to consist of distinct bands corresponding to the photoreceptor OS tips, RPE, and BM. The normative measurements reported herein may aid in future investigations of outer retinal changes in age-related macular degeneration and other diseases.

Acknowledgments

The authors thank Christine A. Curcio and Anita E. Hendrickson for permission to reproduce the histology images.

Supported by National Eye Institute Grants R01-EY11289-21, R01-EY13178-07, and P30-EY008098; National Science Foundation Grant BES-0522845 and a Graduate Research Fellowship (VJS); Air Force Office of Scientific Research Medical Free Electron Laser Program contract FA9550-040-1-0046; the Massachusetts Lions Eye Research Fund; the Eye and Ear Foundation (Pittsburgh, PA); and an unrestricted grant and a Medical Student Eye Research Fellowship from Research to Prevent Blindness (RC). JGF and JSS receive royalties from intellectual property licensed by MIT to Carl Zeiss Meditec, Inc.

References

1. Huang D, Swanson EA, Lin CP, et al. Optical coherence tomography. Science 1991;(5035):1178–1181. [PubMed: 1957169]
2. Puliafito CA, Hee MR, Lin CP, et al. Imaging of macular diseases with optical coherence tomography. Ophthalmology 1995;102(2):217–229. [PubMed: 7862410]
3. Schuman, JS.; Puliafito, CA.; Fujimoto, JG. Optical Coherence Tomography of Ocular Diseases. 2nd ed.. Slack Inc.; Thorofare, NJ: 2004.
4. Ishikawa H, Stein DM, Wollstein G, et al. Macular segmentation with optical coherence tomography. Invest Ophthalmol Vis Sci 2005;46(6):2012–2017. [PubMed: 15914617]
5. Piccolino FC, de la Longrais RR, Ravera G, et al. The foveal photoreceptor layer and visual acuity loss in central serous chorioretinopathy. Am J Ophthalmol 2005;139(1):87–99. [PubMed: 15652832]
6. Villate N, Lee JE, Venkatraman A, Smiddy WE. Photoreceptor layer features in eyes with closed macular holes: optical coherence tomography findings and correlation with visual outcomes. Am J Ophthalmol 2005;139(2):280–289. [PubMed: 15733989]
7. Drexler W, Morgner U, Kartner FX, et al. In vivo ultrahigh-resolution optical coherence tomography. Opt Lett 1999;24(17):1221–1223. [PubMed: 18073990]
8. Drexler W, Morgner U, Ghanta RK, et al. Ultrahigh-resolution ophthalmic optical coherence tomography. Nat Med 2001;7(4):502–507. [PubMed: 11283681]

9. Drexler W, Sattmann H, Hermann B, et al. Enhanced visualization of macular pathology with the use of ultrahigh-resolution optical coherence tomography. Arch Ophthalmol 2003;121(5):695–706. [PubMed: 12742848]
10. Ko TH, Fujimoto JG, Duker JS, et al. Comparison of ultrahigh- and standard-resolution optical coherence tomography for imaging macular hole pathology and repair. Ophthalmology 2004;111 (11):2033–2043. [PubMed: 15522369]
11. Wollstein G, Paunescu LA, Ko TH, et al. Ultrahigh-resolution optical coherence tomography in glaucoma. Ophthalmology 2005;112(2):229–237. [PubMed: 15691556]
12. Ergun E, Hermann B, Wirtitsch M, et al. Assessment of central visual function in Stargardt's disease/fundus flavimaculatus with ultrahigh-resolution optical coherence tomography. Invest Ophthalmol Vis Sci 2005;46(1):310–316. [PubMed: 15623790]
13. Ko TH, Fujimoto JG, Schuman JS, et al. Comparison of ultrahigh- and standard-resolution optical coherence tomography for imaging macular pathology. Ophthalmology 2005;112(11):1922.e1–e15. [PubMed: 16183127]
14. Witkin AJ, Ko TH, Fujimoto JG, et al. Ultra-high resolution optical coherence tomography assessment of photoreceptors in retinitis pigmentosa and related diseases. Am J Ophthalmol 2006;142(6):945–952. [PubMed: 17157580]
15. Cense B, Nassif NA, Chen TC, et al. Ultrahigh-resolution high-speed retinal imaging using spectral-domain optical coherence tomography. Opt Express 2004;12(11):2435–2447. [PubMed: 19475080]
16. Leitgeb RA, Drexler W, Unterhuber A, et al. Ultrahigh resolution Fourier domain optical coherence tomography. Opt Express 2004;12(10):2156–2165. [PubMed: 19475051]
17. Wojtkowski M, Srinivasan VJ, Ko TH, et al. Ultrahigh resolution, high speed, Fourier domain optical coherence tomography and methods for dispersion compensation. Opt Express 2004;12(11):2404–2422. [PubMed: 19475077]
18. Fercher AF, Hitzenberger CK, Kamp G, Elzaiat SY. Measurement of intraocular distances by backscattering spectral interferometry. Opt Commun 1995;117(1–2):43–48.
19. Hausler G, Lindner MW. "Coherence radar" and "spectral radar": new tools for dermatological diagnosis. J Biomed Opt 1998;3(1):21–31.
20. Leitgeb R, Hitzenberger CK, Fercher AF. Performance of Fourier domain vs. time domain optical coherence tomography. Opt Express 2003;11(8):889–894. [PubMed: 19461802]
21. de Boer JF, Cense B, Park BH, et al. Improved signal-to-noise ratio in spectral-domain compared with time-domain optical coherence tomography. Opt Lett 2003;28(21):2067–2069. [PubMed: 14587817]
22. Choma MA, Sarunic MV, Yang CH, Izatt JA. Sensitivity advantage of swept source and Fourier domain optical coherence tomography. Opt Express 2003;11(18):2183–2189. [PubMed: 19466106]
23. Schmidt-Erfurth U, Leitgeb RA, Michels S, et al. Three-dimensional ultrahigh-resolution optical coherence tomography of macular diseases. Invest Ophthalmol Vis Sci 2005;46(9):3393–3402. [PubMed: 16123444]
24. Hangai M, Ojima Y, Gotoh N, et al. Three-dimensional imaging of macular holes with high-speed optical coherence tomography. Ophthalmology 2007;114(4):763–773. [PubMed: 17187861]
25. Srinivasan VJ, Wojtkowski M, Witkin AJ, et al. High-definition and 3-dimensional imaging of macular pathologies with high-speed ultrahigh-resolution optical coherence tomography. Ophthalmology 2006;113(11):2054 e1–e14. [PubMed: 17074565]
26. Zhang Y, Cense B, Rha J, et al. High-speed volumetric imaging of cone photoreceptors with adaptive optics spectral-domain optical coherence tomography. Opt Express 2006;14(10):4380–4394. [PubMed: 19096730]
27. Tripathi R, Nassif N, Nelson JS, Park BH, de Boer JF. Spectral shaping for non-Gaussian source spectra in optical coherence tomography. Opt Lett 2002;27(6):406–408. [PubMed: 18007816]
28. Curcio CA, Sloan KR, Kalina RE, Hendrickson AE. Human photoreceptor topography. J Comp Neurol 1990;292(4):497–523. [PubMed: 2324310]
29. Hitzenberger CK, Trost P, Pak-Wai L, Qienyuan Z. Three-dimensional imaging of the human retina by high-speed optical coherence tomography. Opt Express 2003;11(21):2753–2761. [PubMed: 19471390]

30. Wojtkowski M, Bajraszewski T, Gorczynska I, et al. Ophthalmic imaging by spectral optical coherence tomography. Am J Ophthalmol 2004;138(3):412–419. [PubMed: 15364223]

31. Jiao SL, Knighton R, Huang XR, Gregori G, Puliafito CA. Simultaneous acquisition of sectional and fundus ophthalmic images with spectral-domain optical coherence tomography. Opt Express 2005;13 (2):444–452. [PubMed: 19488371]

32. Koozekanani D, Boyer K, Roberts C. Retinal thickness measurements from optical coherence tomography using a Markov boundary model. IEEE Trans Med Imag 2001;20(9):900–916.

33. Gloesmann M, Hermann B, Schubert C, et al. Histologic correlation of pig retina radial stratification with ultrahigh-resolution optical coherence tomography. Invest Ophthalmol Vis Sci 2003;44(4): 1696–1703. [PubMed: 12657611]

34. Anger EM, Unterhuber A, Hermann B, et al. Ultrahigh resolution optical coherence tomography of the monkey fovea: identification of retinal sublayers by correlation with semithin histology sections. Exp Eye Res 2004;78(6):1117–1125. [PubMed: 15109918]

35. Huang JC, Voaden MJ, Zarbin MA, Marshall J. Morphologic preservation and variability of human donor retina. Curr Eye Res 2000;20(3):231–241. [PubMed: 10694900]

36. Yuodelis C, Hendrickson A. A qualitative and quantitative analysis of the human fovea during development. Vision Res 1986;26(6):847–855. [PubMed: 3750868]

37. Hendrickson A, Drucker D. The development of parafoveal and mid-peripheral human retina. Behav Brain Res 1992;49(1):21–31. [PubMed: 1388798]

38. Packer O, Hendrickson AE, Curcio CA. Photoreceptor topography of the retina in the adult pigtail macaque (Macaca nemestrina). J Comp Neurol 1989;288(1):165–183. [PubMed: 2794135]

39. Curcio CA, Millican CL, Allen KA, Kalina RE. Aging of the human photoreceptor mosaic: evidence for selective vulnerability of rods in central retina. Invest Ophthalmol Vis Sci 1993;34(12):3278–3296. [PubMed: 8225863]

40. Curcio CA, Owsley C, Jackson GR. Spare the rods, save the cones in aging and age-related maculopathy. Invest Ophthalmol Vis Sci 2000;41(8):2015–2018. [PubMed: 10892836]

41. Jackson GR, Owsley C, Curcio CA. Photoreceptor degeneration and dysfunction in aging and age-related maculopathy. Ageing Res Rev 2002;1(3):381–396. [PubMed: 12067593]

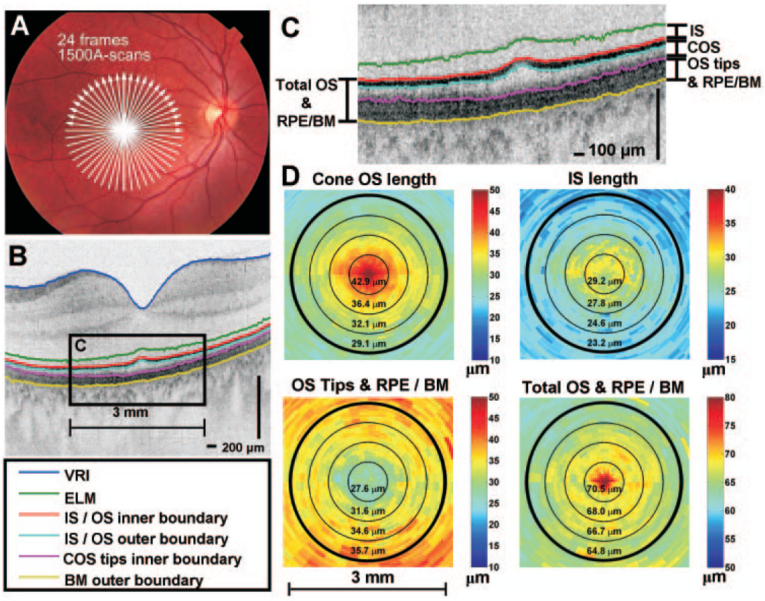

Figure 1.

Example of segmentation performed on the right eye of a 28-year-old man. (**A**) OCT scan protocol of 24 radial 6-mm images (1500 axial scans per image). (**B, C**) A single radial image with segmentation lines is shown. (**D**) Individual retinal layer thicknesses can be calculated and displayed as color maps. Concentric circles with diameters of 0.75, 1.5, 2.25, and 3.0 mm are shown for reference. The interpretation of the outer retina is discussed in detail in the Discussion section.

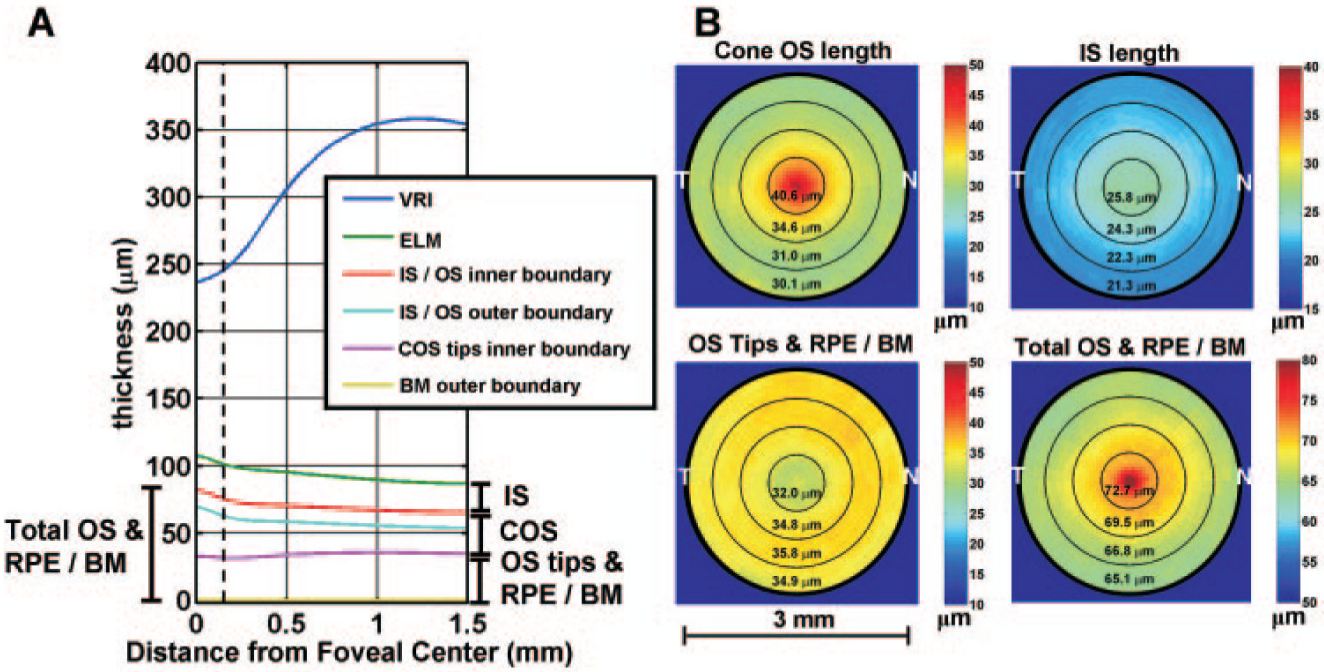

Figure 2.

(**A**) Average dimensions of the outer retina, averaged over all subjects. All measurements are referenced to the outer boundary of BM at 0 μm. The horizontal axis represents distance from the foveal center, and the vertical axis represents the average thickness at a given distance from the foveal center. *Dotted line*: the foveola (0.3 mm diameter). (**B**) Average outer retinal layer thickness maps, averaged over all subjects. The maps show an approximately circularly symmetric pattern, justifying the radial plot shown in (**A**). Although the VRI is not perfectly circularly symmetric, it is shown on the radial plot to enable visualization of the outer retinal morphology relative to the foveal contour.

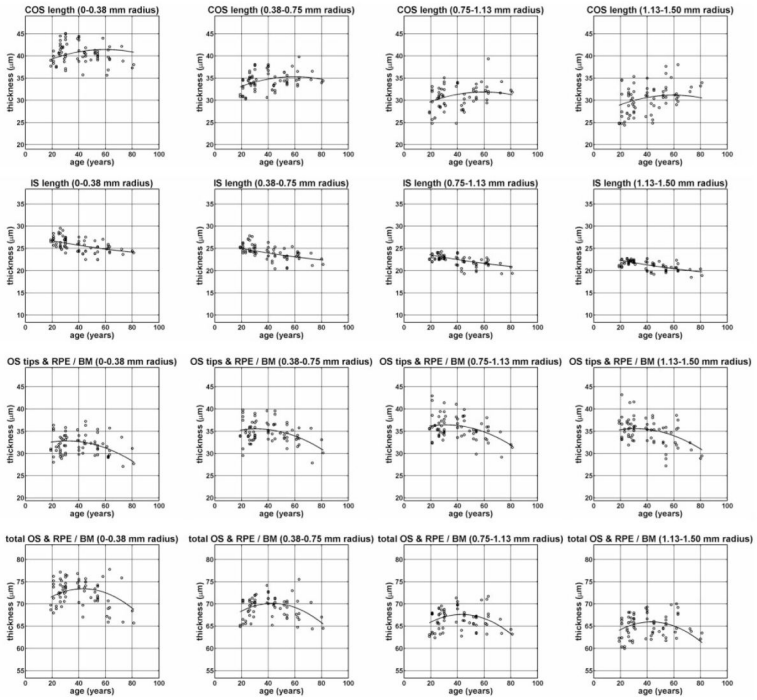

Figure 3.

Scatterplots of average thickness measurements of different features (*rows*), grouped according to annular rings centered on the foveal center (*columns*). The fit obtained from the linear mixed-effects model is shown.

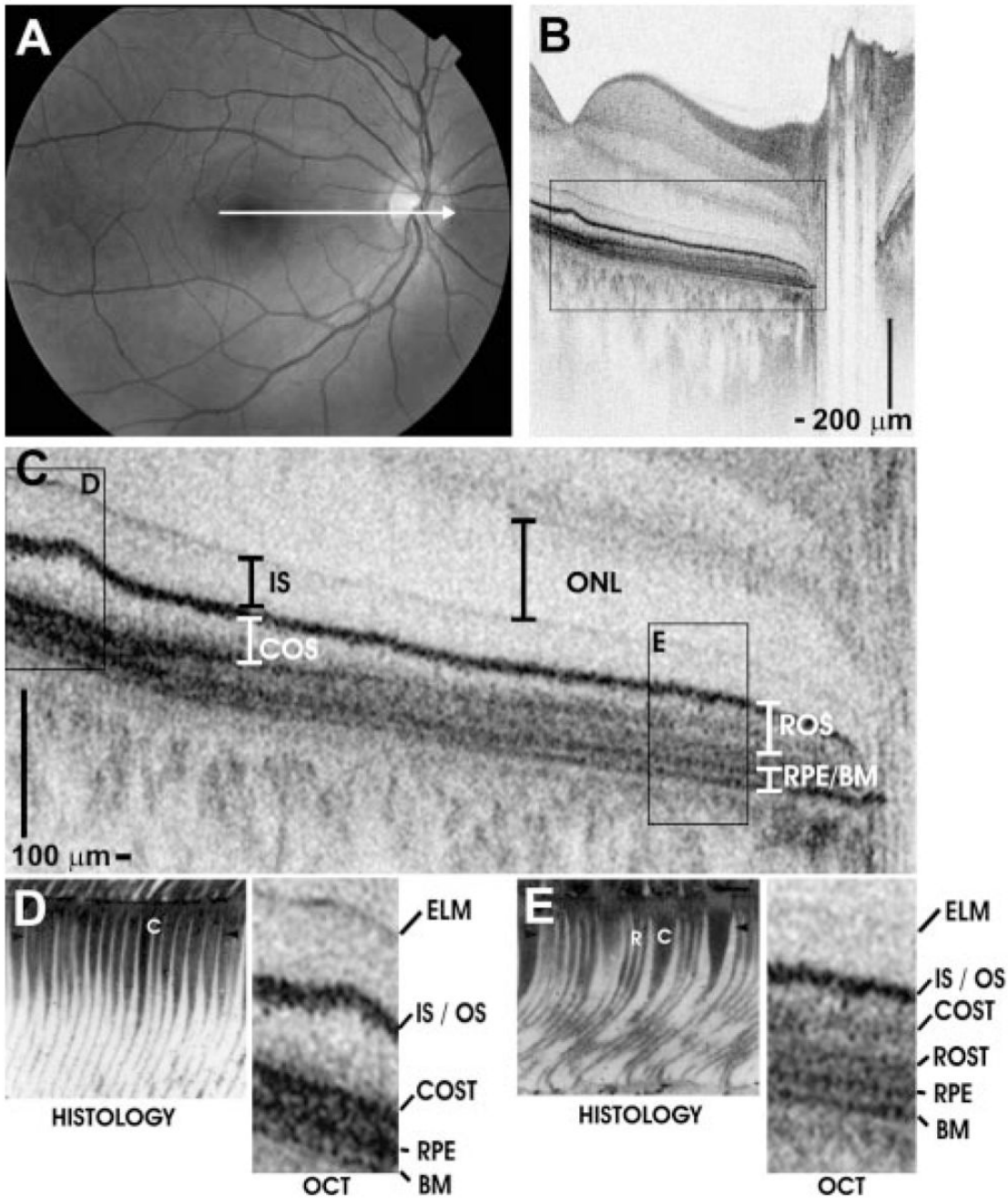

Figure 4.

Papillomacular OCT imaging of the retina of a normal 28-year-old man. (**A**) Fundus photograph showing the OCT scan location. (**B**) Papillomacular OCT image showing the change in outer retinal appearance from the fovea to the near periphery. The OCT image has an axial image resolution of 2.8 μm and consists of 2048 axial scans. (**C**) Enlarged image of *boxed region* shows outer retina in detail, with retinal layers labeled. (**D, E**) Representative histology images from the foveola (**D**) and near periphery (**E**) correspond with UHR OCT. Cones (C) and rods (R) are labeled on the histology images for reference. The histology images are of a different subject and are reproduced with permission.[28]

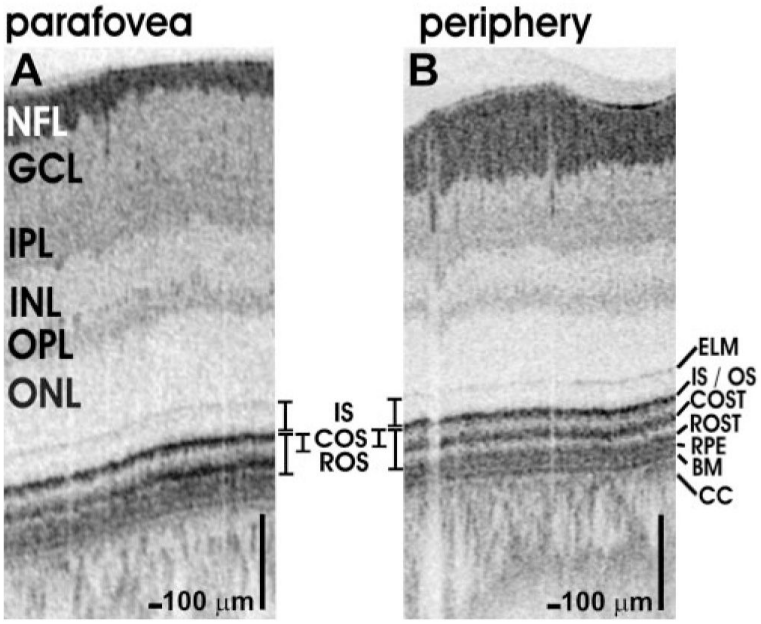

Figure 5.
Comparison of OCT retinal images (~1660 axial scans) from the parafovea (1.5 mm from foveal center, **A**) and periphery (5.2 mm from foveal center and superior to the nerve head, **B**) of a normal 24-year-old man. The retina is thinner peripherally, COS are shorter, and the tips are displaced from the RPE and the ROSTs.

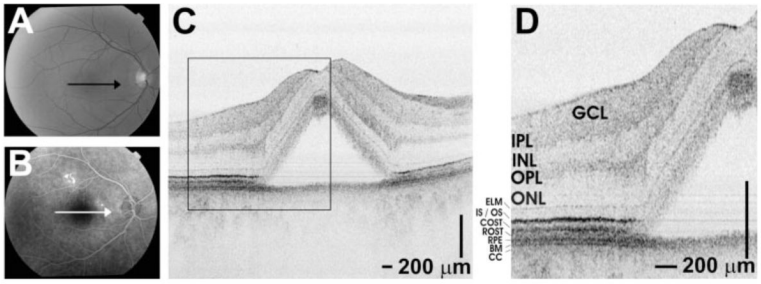

Figure 6.
Case of acute central serous chorioretinopathy. Fundus photograph (**A**) and fluorescein angiogram (**B**) show serous fluid under the macula. The OCT image shows elevation of retina from the RPE. Enlarged image of *boxed region* shows the outer retinal layers in detail.

Table 1

Mixed-Effects Model Parameter Estimates

	COS Length	IS Length	OS Tips and RPE/BM	Total OS and RPE/BM
β_0(μm)	32.9	23.1	35.9	68.8
	(32.0 to 33.7)	(22.5 to 23.7)	(35.1 to 36.8)	(68.0 to 69.5)
$\beta_{1,age}$(μm/year)	4.67E-2	−4.64E-2	−4.43E-2	3.04E-3
	(8.84E-3 to 8.46E-2)	(−7.36E-2 to −1.93E-2)	(−8.26E-2 to −6.11E-3)	(−3.10E-2 to 3.71E-2)
$\beta_{2,age}$(μm/year^2)	−1.37E-3	2.18E-4	−1.91E-3	−3.24E-3
	−3.43E-3 to 6.83E-4)	(−1.22E-3 to 1.66E-3)	(−3.98E-3 to 1.70E-4)	(−5.07E-3 to −1.40E-3)
$\beta_{1,dist}$(μm/mm)	−9.12	−3.92	2.44	−6.64
	(−9.57 to −8.68)	(−4.09 to −3.75)	(1.99 to 2.89)	(−7.00 to −6.29)
$\beta_{2,dist}$(μm/mm^2)	9.65	0.98	−6.32	2.83
	(8.46 to 10.83)	(0.53 to 1.44)	(−7.53 to −5.11)	(1.87 to 3.80)

Parameter estimates (with 95% CI in parenthesis) for the linear mixed-effects model fit shown in Figure 3. The variable *r* represents the outer radius of the annulus. All measurements have negative linear distance slopes and positive quadratic distance slopes, with the exception of the OS tips and RPE/BM measurement, which has a positive linear distance slope and a negative quadratic distance slope. The IS length measurement and the total OS and RPE/BM measurement have relatively weak distance curvatures, whereas the COS length measurement and the OS tips and RPE/BM measurement have strong distance curvature.

* Baseline fixed effects = $\beta_0 + \beta_{1,age} \times (age - 42.7\ years) + \beta_{2,age} \times (age - 42.7\ years)^2 + \beta_{1,dist} \times (r - 0.938\ mm) + \beta_{2,dist} \times (r - 0.938\ mm)^2$.